Solitary Waves on Thin Falling Films in the Very Low Forcing Frequency Limit

Ramesh Raju Mudunuri and Vemuri Balakotaiah
Dept. of Chemical Engineering, University of Houston, Houston, TX 77204

DOI 10.1002/aic.11015
Published online October 4, 2006 in Wiley InterScience (www.interscience.wiley.com).

A new family of traveling waves on falling films obtained in the limit of zero pulsing frequency is presented and analyzed. A new two-mode model that can describe the dynamics of waves for Weber numbers greater than unity is derived and validated. The speed (Ce) and peak height (h_{max}) relation for solitary waves is predicted to be linear by the model and its predictions are in excellent agreement with experimental data. Weakly nonlinear analysis of the new wave family, using the new two-mode model, showed that the speed to peak height relation of these solitary waves is linear with slope $\sqrt{3}$, which is in close agreement with experimental results. Furthermore, the local bifurcation analysis shows that the relation $Ce - 3 = \sqrt{3}(h_{max} - 1)$ is independent of the angle of the inclination as well as fluid properties and flow rate. © 2006 American Institute of Chemical Engineers *AIChE J,* 52: 3995–4003, 2006

Keywords: solitary waves, thin films, gas-liquid flows, wavy films, interfacial turbulence

Introduction

Thin falling films have been studied for more than half a century since the pioneering work of Kapitza.[1] The wavy surface exhibits complex spatiotemporal dynamics and structures such as periodic, solitary, and chaotic waves have been observed.[2] Experiments involving falling films can be categorized into two kinds: (1) where the inlet flow rate or film thickness is periodically pulsed at one or more frequencies and (2) where waves evolved naturally and were excited as a result of ambient noise. In pulsing experiments, waves evolved into periodic or solitary waves depending on the monochromatic pulsing frequencies. At low frequency, solitary waves were observed. The speed and height of solitary waves, as measured in experiments, were found to correlate linearly.[3,4] In this article, we first derive a new two-equation model in terms of local film thickness (h) and flow rate per unit wall width (q) and validate it by (1) comparing the model simulations with direct numerical simulations (DNS) of the Navier–Stokes equations and by (2) calculating the relation between the speed and peak height of solitary waves. Further, we present a new family of solitary waves obtained in the limit of zero pulsing frequency and develop a relation between the speed and peak height of solitary waves of the new family.

In Figure 1, we establish the coordinate system for the two-dimensional (2D) flow. The fluid flows down a plane, inclined at an angle β to the horizontal. The x-axis is along the wall and the y-axis is transverse to the primary flow. The dynamic, deformable interface may change shape as the film flows down.

A New Two-Equation Model

The 2D Navier–Stokes (NS) equations admit a trivial flat film solution known as the Nusselt solution, where flow is steady, one-dimensional (1D) with a parabolic velocity profile and hydrostatic pressure profile. If h_N is the Nusselt film thickness, then Nusselt velocity is given by

$$u = \frac{g \sin(\beta) h_N^2}{\nu}\left[\frac{y}{h_N} - \frac{1}{2}\left(\frac{y}{h_N}\right)^2\right]$$

where g is acceleration arising from gravity and ν is the kinematic viscosity. The wall holds back the fluid from accel-

Correspondence concerning this article should be addressed to V. Balakotaiah at bala@uh.edu.

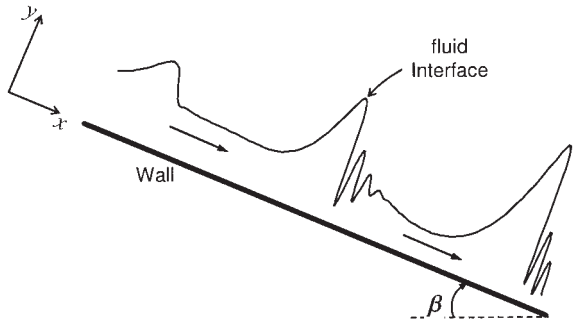

Figure 1. 2D free-falling liquid film flowing down a plane inclined at an angle β to the horizontal.

Flow is attributed to gravity. The schematic shown is the surface profile of a 54% glycerin solution flowing down a plane inclined at 6.4° close to the inlet, when the inlet flow rate was periodically pulsed at 1.5 Hz.

erating because of gravity. It has been observed that the flat film becomes unstable through long waves.[1] Such a scenario of formation of long waves from the flat film would prompt a regular perturbation approach around the Nusselt solution. Such an approach has been used extensively and is termed *long-wave expansion*. Following the long-wave expansion, we do a perturbation expansion of the governing NS equations and boundary conditions around the flat film solution. If λ is the wavelength of the perturbed surface, a long-wave parameter $\alpha = 2\pi h_N/\lambda$ characterizes departure from the Nusselt solution. Using h_N, $u_N = g\sin(\beta)h_N^2/(3\nu)$ (average Nusselt velocity), h_N/u_N, and $\mu u_N/(4h_N)$ as the characteristic length, velocity, time, and pressure, respectively, the system is governed by the following independent dimensionless parameters, the Reynolds number

$$\mathrm{Re} = \frac{4u_N h_N}{\nu} = \frac{4g\sin(\beta)h_N^3}{3\nu^2}$$

the Weber number

$$\mathrm{We} = \frac{\sigma}{\rho u_N^2 h_N} = \frac{9\sigma\mu^2}{\rho^3[g\sin(\beta)]^2 h_N^5}$$

and the inclination angle β. σ and μ are the surface tension and viscosity, respectively. Another dimensionless parameter, the Kapitza number, $\mathrm{Ka} = \sigma\rho^{1/3}/\{[g\sin(\beta)]^{1/3}\mu^{4/3}\}$, which is independent of the flow conditions, is also used. Note that the Re, Ka, and We are related by $\mathrm{We} = 3^{1/3}4^{5/3}(\mathrm{Ka}/\mathrm{Re}^{5/3})$. In the spirit of long-wave expansion, the x coordinate is made dimensionless with respect to $\lambda/(2\pi)$ and resulting dimensionless equations are given by

$$\mathrm{Re}\left(\frac{\partial u}{\partial t} + \alpha u\frac{\partial u}{\partial x} + v\frac{\partial u}{\partial y}\right) = -\alpha\frac{\partial p}{\partial x} + 12 + 4\left(\alpha^2\frac{\partial^2 u}{\partial x^2} + \frac{\partial^2 u}{\partial y^2}\right) \quad (1)$$

$$\mathrm{Re}\left(\frac{\partial v}{\partial t} + \alpha u\frac{\partial v}{\partial x} + v\frac{\partial v}{\partial y}\right) = -\frac{\partial p}{\partial y} - 12\cot(\beta) + 4\left(\alpha^2\frac{\partial^2 v}{\partial x^2} + \frac{\partial^2 v}{\partial y^2}\right) \quad (2)$$

$$\alpha\frac{\partial u}{\partial x} + \frac{\partial v}{\partial y} = 0 \quad (3)$$

$$\alpha\frac{\partial q}{\partial x} + \frac{\partial h}{\partial t} = 0 \qquad \text{where } q = \int_0^h u\,dy \quad (4)$$

Equations 1 and 2 are the x- and y-momentum balance equations, whereas Eqs. 3 and 4 are the continuity equation and kinematic condition. The kinematic condition maintains that the fluid is trapped between the impermeable wall and the fluid–gas interface. Here, the wavenumber α appears in all the terms containing the streamwise derivatives stemming from the above-mentioned scaling of the x coordinate.

The boundary conditions in dimensionless form are given by

$$u = v = 0 \qquad @y = 0 \quad (5)$$

$$\left(\frac{\partial u}{\partial y} + \alpha\frac{\partial v}{\partial x}\right)(1 - \alpha^2 h_x^2) + 2\alpha h_x\left(\frac{\partial v}{\partial y} - \alpha\frac{\partial u}{\partial x}\right) = 0 \qquad @y = h \quad (6)$$

$$p + 8\left(\frac{\partial u}{\partial y} + \alpha\frac{\partial v}{\partial x}\right)\frac{\alpha h_x}{(1 + \alpha^2 h_x^2)} + 8\alpha\frac{\partial u}{\partial x}\frac{(1 - \alpha^2 h_x^2)}{(1 + \alpha^2 h_x^2)} + \mathrm{ReWe}\frac{\alpha^2 h_{xx}}{(1 + \alpha^2 h_x^2)^{3/2}} = 0 \qquad @y = h \quad (7)$$

Equation 5 is the no-slip boundary condition. Equations 6 and 7 are the tangential and normal stress continuity boundary conditions, respectively. Note that when $\alpha = 0$, the kinematic boundary condition simply states

$$\frac{\partial h}{\partial t} = 0$$

which is the evolution equation for the Nusselt solution. A perturbation expansion in velocities and pressure is introduced:

$$u = u_0 + \alpha u_1 + \alpha^2 u_2 + \cdots \quad (8)$$

$$v = v_0 + \alpha v_1 + \alpha^2 v_2 + \cdots \quad (9)$$

$$p = p_0 + \alpha p_1 + \alpha^2 p_2 + \cdots \quad (10)$$

Before introducing the above expansions in the NS equations and obtaining equations at different orders, one has to assume some order of magnitude for the dimensionless parameters Re and We in terms of α. Such a dependency is termed *scaling*. If Re is independent of α, then $\mathrm{Re} \sim O(1)$; if Re is small, then a scaling $\mathrm{Re} \sim O(\alpha)$ can be used. Traditionally, $\alpha^2\mathrm{We} \sim O(1)$,

known as long-wave scaling, has been used for We. We argue here that there is a natural scaling for thin film long-wave instabilities. As the wavelength $\lambda \to \infty$ ($\alpha \to 0$), we expect the free surface to be flat and in that limit we should be able to obtain the Nusselt flat film solution from the above set of equations. For nonzero α, when long waves appear on the film, the surface curvature is finite and the surface tension forces become active. For $\alpha \neq 0$, surface tension forces contribute to the pressure inside the fluid at the surface, or the surface tension effect should show up at first order in the perturbation. Therefore, in Eqs. 10 and 7 the surface tension contribution $\mathrm{ReWe}\alpha^2\{h_{xx}/[(1 + \alpha^2 h_x^2)^{3/2}]\}$ has to be order one in α, or $\mathrm{ReWe}\alpha \sim O(1)$. This scaling would be referred to as global scaling and requires that the surface tension affect the pressure as soon as waves appear. For thin film long wave instabilities, there is a natural scaling given by $\alpha\mathrm{ReWe} \sim O(1)$.

As assumed by Shkadov,[5] we assume a self-similar velocity profile, and express the axial velocity as

$$u = 3[a_0(x, t) + \alpha a_1(x, t) + \alpha^2 a_2(x, t)]\left[h(x, t)y - \frac{y^2}{2}\right]$$

$$u_0 = 3a_0\left(hy - \frac{y^2}{2}\right)$$

$$u_1 = 3a_1\left(hy - \frac{y^2}{2}\right)$$

$$u_2 = 3a_2\left(hy - \frac{y^2}{2}\right) \tag{11}$$

where a_0, a_1, a_2, and h are all functions of axial coordinate x and time t. The velocity modes a_0, a_1, and a_2 are related to the flow rate by

$$q = \int_0^h u dy \qquad a_0 + \alpha a_1 + \alpha^2 a_2 = \frac{q(x, t)}{h(x, t)^3} \tag{12}$$

The assumed form of the axial velocity can be substituted in the continuity equation given by Eq. 3 to solve for the transverse velocity, $v(x, y, t)$. Using the y-momentum balance and the normal stress boundary conditions, we may solve for the pressure across the film. This pressure solution is substituted in the x-momentum balance. The x-momentum equations are suitably integrated in the transverse direction and this step is known as *projection*. Ruyer-Quil and Manneville[6] recommend a Galerkin projection. Using a Galerkin projection, at different orders we get corresponding evolution equations for different a values from [with $f = hy - (y^2/2)$]

$$\int_0^h (fN_i)dy = 0 \qquad i = 0, 1\cdots \tag{13}$$

where N_i represents the terms of order i in the x-momentum equation.

At order two, the inhomogeneous boundary condition is handled as

$$\int_0^h \left(f\frac{\partial^2 u_2}{\partial y^2}\right)dy = \left(f\frac{\partial u_2}{\partial y}\right)\Big|_h + \int_0^h (f'u_2)dy \tag{14}$$

At second order, after integration, the resulting equation contains a mixed derivative of a_0, coming from the $\partial v_1/\partial t$ term in the governing equation for pressure p_1. We may then use the evolution equation at order zero, which is simply an evolution equation for a_0, to replace $\partial a_0/\partial t$ in the evolution equation for a_2 to handle the mixed derivative of a_0.

Adding all the projection steps leads to a composite equation that relates the evolution of a_i ($i = 0, 1, 2$). In conjunction with the kinematic BC and Eq. 12, which relates the a_i' values to flow rate and retaining terms up to order two in α, we may eliminate values of a_i' and write the composite equation in terms of q, h, and their derivatives. After rescaling x with h_N, the final expression is an evolution equation in q and when coupled with the kinematic boundary conditions closes the set. For inclined films, the final evolution equation (EE) with scaling $\mathrm{Re} \sim O(1)$ and $\alpha\mathrm{ReWe} \sim O(1)$ reads

$$\frac{2}{5}\mathrm{Re}q_t = 4h - 4\frac{q}{h^2} - 4Bhh_x + \frac{18}{35}\mathrm{Re}\frac{q^2h_x}{h^2} - \frac{34}{35}\mathrm{Re}\frac{qq_x}{h} - \frac{339}{70}\frac{h_xq_x}{h} - \frac{9}{7}hh_x^2 + \frac{373}{70}\frac{qh_x^2}{h^2} - \frac{41}{84}h^2h_{xx} - \frac{2837}{420}\frac{qh_{xx}}{h} + \frac{449}{70}q_{xx} + \frac{1}{3}\mathrm{ReWe}hh_{xxx} \tag{15a}$$

$$h_t + q_x = 0 \tag{15b}$$

where $B = \cot\beta$. If we use the scaling $\mathrm{Re} \sim O(\alpha)$ and $\mathrm{ReWe}\alpha \sim O(1)$, we arrive at the equations derived in Ruyer-Quil and Manneville.[6] Our model equations (Eqs. 15a and 15b) are free from finite time blow up (as discussed by Pumir et al.[7]) exhibited by single evolution or surface equations and compare favorably with linear stability calculations of the Orr–Sommerfield equations.[8] The model is valid for Weber numbers greater than unity.[8] We use the model equations given by Eq. 15 to analyze the dynamics of falling films.

Validation of the Model

To validate the model, we compare the model predictions with the DNS of Nosoko and Miyara,[9] for vertically falling water films. To simulate the monochromatic pulsing experiments, periodic monochromatic pulses were introduced at the inlet (also the origin of the coordinate system) through:

$$q(0, t) = 1 + \delta\sin(2\pi ft) \tag{16}$$

$$h(0, t) = [q(0, t)]^{1/3} \tag{17}$$

where δ is the amplitude of the periodic disturbance. Equation 17 simply assumes that the introduced flow profile is Nusselt like, where $q = h^3$. The initial conditions given by

$$q(x, 0) = 1 \qquad h(x, 0) = 1 \tag{18}$$

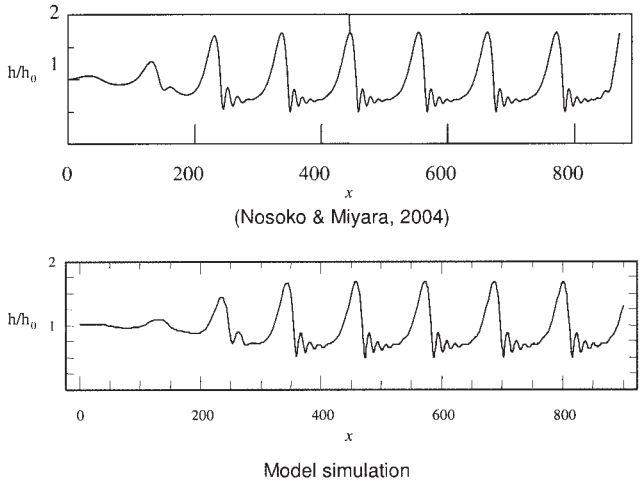

Figure 2. Comparison of direct numerical simulations of the Navier–Stokes equations and simulation wave traces for water films with Re = 64.4, We = 47.43, β = 90°, and f = 14 Hz.

The dimensionless thickness is shown on the y-axis and the dimensionless downstream distance is shown on the x-axis.

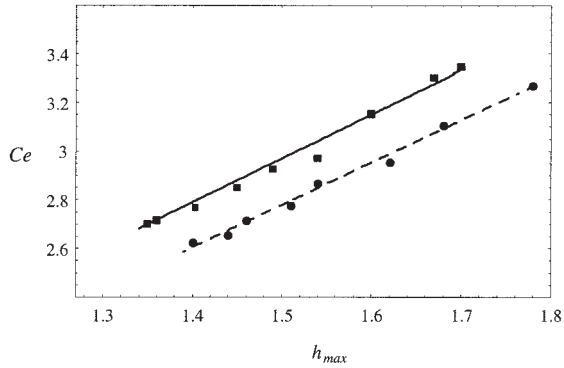

Figure 4. Comparison of celerity and peak height of solitary waves.

Ka = 488 and β = 8°. The solid line (Re = 80.533, We = 4.72) and the dashed line (Re = 67.2, We = 6.38) are results from time simulations of the Eq. 15 system. Experimental data represented by squares (Re = 80.533, We = 4.72) and disks (Re = 67.2, We = 6.38) have been extracted from Figure 10 of Liu and Gollub.[4] The solid line has a slope 1.74, whereas the dashed line has a slope 1.8. In the text, we show that the theoretical slope is estimated to be $\sqrt{3}$.

were used, which correspond to the Nusselt film. The other boundary conditions used were, $q_x(0, t) = 0$, $h_x(0, t) = 0$, and $h_x(L, t) = 0$, where L is the length of the computational domain. In Figures 2 and 3, we compare the DNS results with those of the model. The linear and nonlinear growth regions are shown. The saturated wave structure is well captured by the model. In Figure 2, the waves evolve into solitary waves, whereas in Figure 3, highly interacting waves are observed.

Experimental measurements showed that the speed and peak height of solitary waves correlated linearly.[3,4] To find the speed and peak height of solitary waves as predicted by the model, we carried out numerical simulations by varying the monochromatic pulsing frequency of inlet pulses for fixed values of Re, We, and β. The speed and peak height of the solitary waves

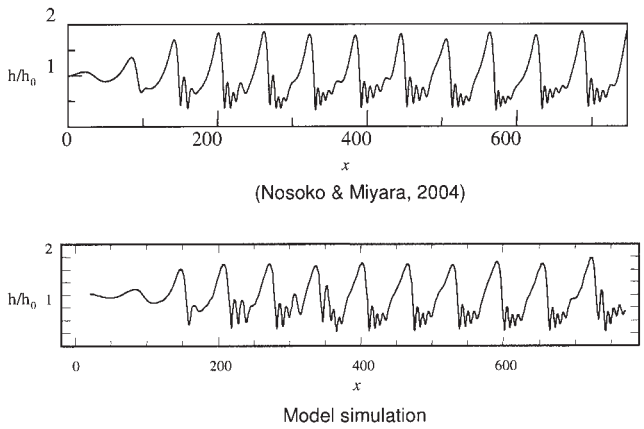

Figure 3. Comparison of direct numerical simulations of the Navier–Stokes equations and simulation wave traces for water films with Re = 206, We = 6.83, β = 90°, and f = 25 Hz.

The dimensionless thickness is shown on the y-axis and the dimensionless downstream distance is shown on the x-axis.

increased with decreasing frequency. In Figure 4, we compare the model predictions with the experimental data of Liu and Gollub.[4] In the figure, the experimental data points represented by squares (Re = 80.533, We = 4.72) and disks (Re = 67.2, We = 6.38) were extracted from Figure 10 of Liu and Gollub.[4] The model predictions (obtained by time simulations of Eq. 15) are given by the solid line (Re = 80.533, We = 4.72) and the dashed line (Re = 67.2, We = 6.38). The model predicts a linear relation between the speed and peak height of solitary waves. Slopes of the solid line and the dashed line are 1.74 and 1.8, respectively. From the figure, it is clear that the model predictions are in quantitative agreement with experimental data (note that there are notational differences between those in Liu and Gollub[4] and those herein). Below, we present a new family of solitary waves obtained in the limit of zero pulsing frequency. The slope of the linear relation between the speed and peak height of the solitary waves of the new family is shown to be $\sqrt{3}$ for both vertical and inclined films.

Limit of Pulsing Frequency Going to Zero

The limiting case of pulsing frequency going to zero is considered in this section. It is difficult to do experiments in the limit of very low frequencies.[10,11] It is also difficult to do time simulations because we would require a long spatial domain, and then solve for long times. Fortunately, the case of $f \rightarrow 0$ can be analyzed without resorting to time simulations.

It had been noticed in experiments and simulations that the solitary waves attain a steady shape and speed. The waves generated in the limit of $f \rightarrow 0$ can be studied in a steady traveling coordinate system. The linear stability envelope (critical/neutral wave number, α_c vs. 1/We diagram) consists of two curves, α_c and $\alpha = 0$, with both curves intersecting at the critical flow rate. The limit of $f \rightarrow 0$ corresponds to $\alpha = 0$ and $Ce = 3$ curves of the linear stability diagram.

Assuming that Ce is the celerity of the steady traveling wave and $z = x - Cet$, the kinematic condition is transformed to $q - Ceh = q_0$, where q_0 is the integration constant. In the limit $f \rightarrow$

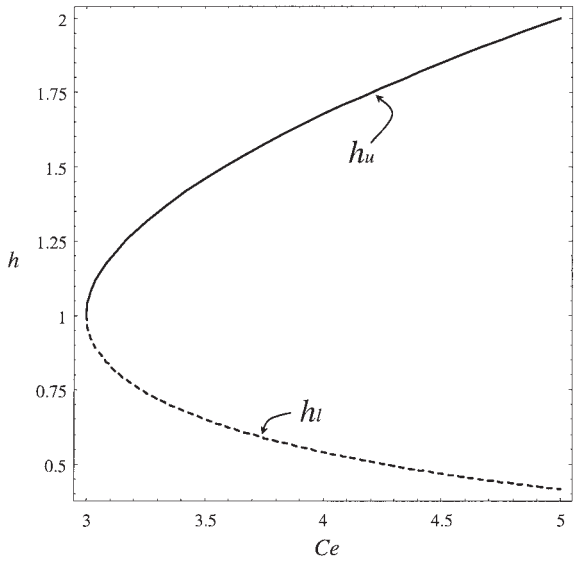

Figure 5. Plot showing the fixed points of flow given by Eq. 20, which are also the solutions of Eq. 22.

The upper branch h_u is given by Eq. 23, whereas the lower branch h_l is given by Eq. 24.

0, the point given by $h = 1$ and $Ce = 3$ is a solution to the kinematic condition ($\alpha = 0$ in the linear stability diagram corresponds to $h = 1$). By substituting, $h = 1$ and $Ce = 3$ in the kinematic condition, we obtain

$$q - Ceh + 2 = 0 \tag{19}$$

On eliminating q from Eq. 19 and the model equations for vertically falling films in the steady traveling system, we arrive at the following equation for h:

$$-\frac{8}{h^2} + \frac{4Ce}{h} - 4h + \frac{2}{35}Ce^2\mathrm{Re}h_z - \frac{72\mathrm{Re}h_z}{35h^2} + \frac{4Ce\mathrm{Re}h_z}{35h} + \frac{373h_z^2}{35h^2} - \frac{17Ceh_z^2}{35h} + \frac{9hh_z^2}{7} + \frac{143Ceh_{zz}}{420} - \frac{2837h_{zz}}{210h} + \frac{41h^2h_{zz}}{84} - \frac{1}{3}h\mathrm{ReWe}h_{zzz} = 0 \tag{20}$$

The third-order Eq. 20 can be recast as a set of three first-order equations, given by

$$\frac{d}{dz}\begin{pmatrix}\mathrm{h1}\\ \mathrm{h2}\\ \mathrm{h3}\end{pmatrix} = f(\boldsymbol{h}) = \frac{d}{dz}(\boldsymbol{h}) \tag{21}$$

where, $\mathrm{h1} = h$, $\mathrm{h2} = h_z$, and $\mathrm{h3} = h_{zz}$. We use this equation for computations in this section. The fixed points of Eq. 20 are obtained as solutions to

$$h^3 - Ceh + 2 = 0 \tag{22}$$

which are shown in Figure 5. The fixed-points map consists of two branches that intersect at $(h, Ce) = (1, 3)$. The branch with $0 < h < 1$ will be termed the lower branch (h_l) and the branch with $h > 1$ is termed the upper branch (h_u). The upper branch is stable depending on the parameters Re, We, and Ce. The lower branch is always unstable. The upper and lower branches are given, respectively, by

$$h_u = \frac{3^{1/3}Ce + (-9 + \sqrt{81 - 3Ce^3})^{2/3}}{3^{2/3}(-9 + \sqrt{81 - 3Ce^3})^{1/3}} \tag{23}$$

and

$$h_l = \frac{(-3)^{2/3}Ce - (-3)^{1/3}(-9 + \sqrt{81 - 3Ce^3})^{2/3}}{3(-9 + \sqrt{81 - 3Ce^3})^{1/3}} \tag{24}$$

To verify the stability of the upper branch h_u, given that Ce is varied for a given Re and We, we linearize Eq. 20 and obtain the following expression:

$$\frac{d}{dz}(\boldsymbol{h}_u + \boldsymbol{\eta}) = f(\boldsymbol{h}_u + \boldsymbol{\eta}) = A(\boldsymbol{h}_u)\boldsymbol{\eta} = \frac{d}{dz}(\boldsymbol{\eta}) \tag{25}$$

where the matrix A has a generic form

$$A = \begin{bmatrix} 0 & 1 & 0 \\ 0 & 0 & 1 \\ e_1 & e_2 & e_3 \end{bmatrix} \tag{26}$$

e_1, e_2, and e_3 are model dependent and for our model given by Eq. 20, e_i values are given by

$$e_1 = \frac{10080 - 3360Ceh_u}{140\mathrm{ReWe}h_u^4} \tag{27}$$

$$e_2 = \frac{-864\mathrm{Re}h_u + 48Ce\mathrm{Re}h_u^2 + 24Ce^2\mathrm{Re}h_u^3}{140\mathrm{ReWe}h_u^4} \tag{28}$$

$$e_3 = \frac{-5674h_u^2 + 143Ceh_u^3 + 205h_u^5}{140\mathrm{ReWe}h_u^4} \tag{29}$$

Matrix A, whose eigenvalues determine the stability of the branches, is a function of celerity Ce, Re, and We (h_u is itself a function of Ce). A has three negative eigenvalues for $Ce = 3$ and $\mathrm{Re} > 0$. As we increase Ce, the branch h_u undergoes Hopf bifurcation. On further increasing the celerity, we reach a homoclinic orbit, which corresponds to a solitary wave. The Hopf celerities are given by the following implicit equation:

$$\mathrm{We}[19{,}600h_u(-3 + Ce_{\mathrm{Hopf}}h_u)] = (204{,}264 - 16{,}496Ce_{\mathrm{Hopf}}h_u - 5388Ce_{\mathrm{Hopf}}^2h_u^2 - 7380h_u^3 + 143Ce_{\mathrm{Hopf}}^3h_u^3 + 410Ce_{\mathrm{Hopf}}h_u^4 + 205Ce_{\mathrm{Hopf}}^2h_u^5) \tag{30}$$

Ce_{Hopf} depends only on the Weber number (We). Hopf celerities of various models for different values of We are shown in Figure 6. Hopf celerities reach an asymptotic value for small Weber numbers. Beyond the Hopf celerity, with increasing

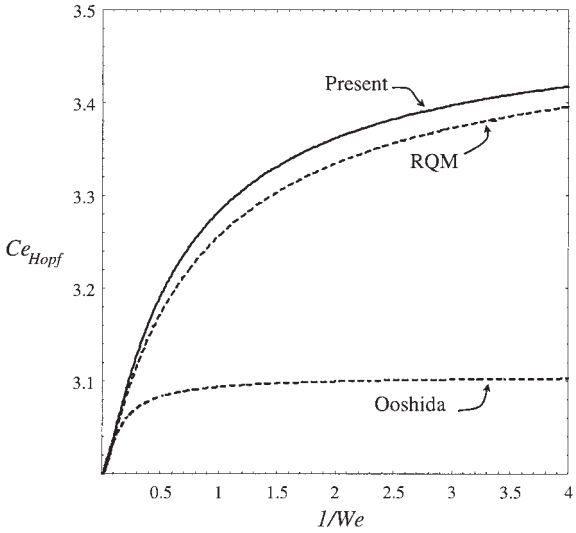

Figure 6. Hopf celerities vs. 1/We, for different model equations.

"Present" refers to Eq. 15, whereas "RQM" refers to the model proposed in Ruyer-Quil and Manneville[6]; "Ooshida" refers to the model proposed in Ooshida.[14]

celerity, on integrating Eq. 20, we hit the homoclinic orbit. These orbits sit on h_l, given by Eq. 24, as substrate. These solitary waves have a substrate that is lower than the Nusselt film thickness and travel with speeds that always exceed 3. In Figures 7 and 8, homoclinic orbits for different parameter ranges are shown. The complexity of the waves increases as one increases the Kapitza number (Ka). For small Ka, as in Figure 7, the solitary wave is characterized by the near absence of capillary waves preceding the main hump. As we increase the Kapitza number, capillary waves in increasing number and

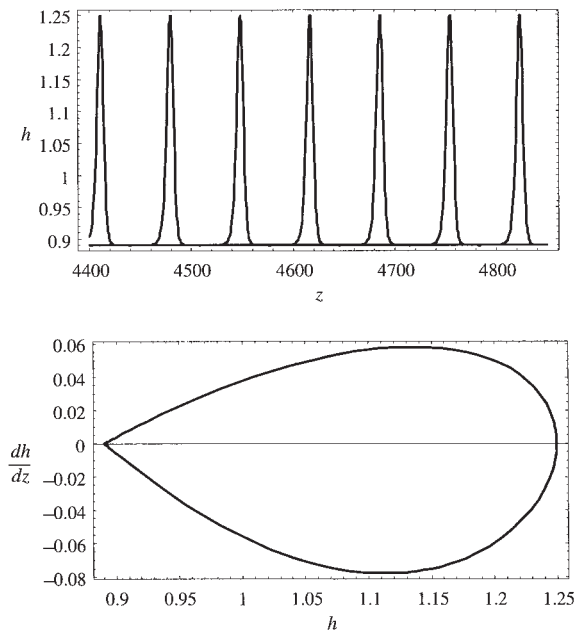

Figure 7. Wave profile and its phase diagram corresponding to a solitary wave, for Ka = 1 and Re = 1, β = 90°.

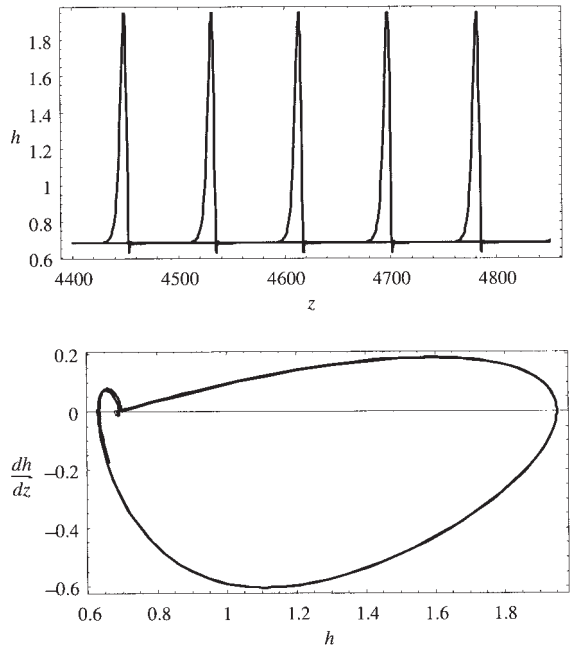

Figure 8. Wave profile and its phase diagram corresponding to a solitary wave, for Ka = 14.89 and Re = 13.74, β = 90°.

intensity appear before the main hump, as shown in Figure 8. Figures 7 and 8 also indicate that the wave structure becomes complex with increasing Kapitza number. For fixed Reynolds and Kapitza numbers, on increasing the celerity from 3, the upper branch h_u undergoes a Hopf bifurcation at Ce_{Hopf}. On further increasing the celerity, we arrive at the homoclinic orbit. In Figure 9, we show bifurcation diagrams where the

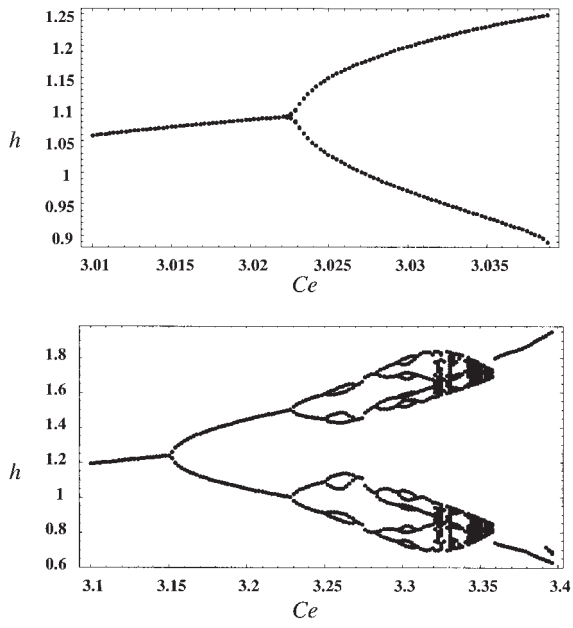

Figure 9. Bifurcation diagram showing the transition from Hopf bifurcation to the homoclinic orbit.

Top: Ka = 1 and Re = 1, β = 90°. Bottom: Ka = 14.89 and Re = 13.74, β = 90°.

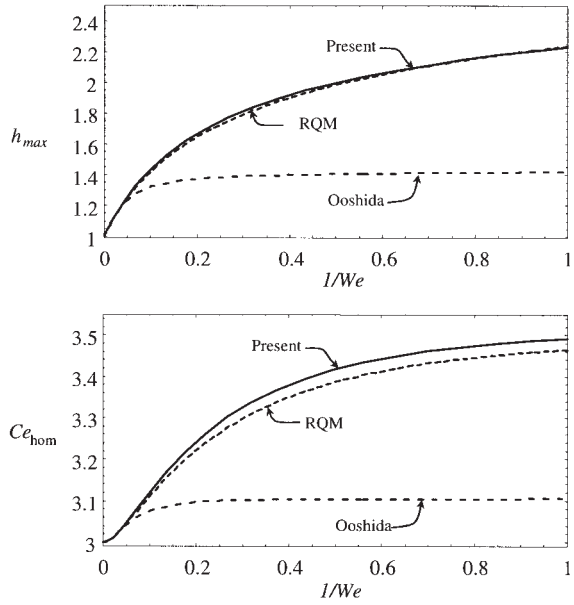

Figure 10. Homoclinic celerities and peak height of the corresponding solitary waves for Ka = 10, β = 90°, predicted by different models, for varying We.

Top: peak heights for different flow rates. Bottom: homoclinic celerites corresponding to the solitary waves shown in the top diagram. "Present" refers to Eq. 15, whereas "RQM" refers to model proposed in Ruyer-Quil and Manneville[6]; "Ooshida" refers to the model proposed in Ooshida.[14]

local minimum and maximum for a given celerity are shown. The top diagram of Figure 9 shows that the transition from Hopf bifurcation to homoclinic orbit is simple for Ka = 1 and Re = 1. For a larger Kapitza number, the transition from Hopf to a homoclinic orbit is through a chaotic window, as shown in the bottom diagram of Figure 9.

The homoclinic celerities and the peak height of the corresponding solitary waves were computed for Ka = 10 for different models for varying flow rates, and are shown in Figure 10. As seen in Figure 10, the celerities lie between 3 and 3.6. The peak heights were found to be <3 for We $\sim O(1)$. Because the model equations based on the long-wave expansion have a limited range of validity, we show the celerities and maximum amplitudes for We > 1.

The relevance of the solitary waves in the low-frequency limit to time simulations is shown in Figure 11. It is seen that the solitary waves can also be computed by time simulations with a small but finite frequency f. For the profiles shown in Figure 11, the solid curve corresponds to time simulations for Re = 20.47, We = 1, f = 0.016, with Ce = 3.492. The dashed curve in Figure 11 is the corresponding homoclinic orbit with Ce = 3.492.

Weakly nonlinear analysis

To derive a useful relation between the speed and peak height of solitary waves in the very low frequency limit, we resort to weakly nonlinear analysis of the model. The center manifold and normal form analysis are used to reduce the ordinary differential equation (ODE) to its simplest form without losing qualitative information.

Near the point 1/We $\rightarrow$ 0 and $Ce \rightarrow 3$ in the parameter space, the linear part of the vector field A is singular and has two zero eigenvalues and a negative eigenvalue. A Taylor series expansion of Eq. 20 up to second order around the flat film solution $(h_1, h_2, h_3) = (1, 0, 0)$ gives

$$\begin{pmatrix} \dot{H}_1 \\ \dot{H}_2 \\ \dot{H}_3 \end{pmatrix} = \mathbf{L}\begin{pmatrix} H_1 \\ H_2 \\ H_3 \end{pmatrix} + \mathbf{Q}(H_1, H_2, H_3) + h\cdot o\cdot t \qquad (31)$$

where $\mathbf{L}$ is given by

$$\mathbf{L} = \begin{bmatrix} 0 & 1 & 0 \\ 0 & 0 & 1 \\ (-24\sqrt{3}\mu)\mathrm{Ca} & \frac{174}{35}\zeta\sqrt{3}\mu - \frac{18\zeta}{5} & \left(\frac{927\sqrt{3}\mu}{35} - 36\right)\mathrm{Ca} \end{bmatrix} \qquad (32)$$

and $\mathbf{Q}$ is given by

$$\mathbf{Q}(H_1, H_2, H_3) = \mathrm{Ca}(96\sqrt{3}\mu - 36)H_1^2 + \left(\frac{522\zeta}{35} - \frac{108}{5}\sqrt{3}\zeta\mu\right)H_2H_1 + \left(\frac{2781}{35} - \frac{5531\sqrt{3}\mu}{70}\right)\mathrm{Ca}H_3H_1 + \left(\frac{1101}{35} - \frac{1017\sqrt{3}\mu}{35}\right)\mathrm{Ca}H_2^2 \qquad (33)$$

where $H_1 = H = h - 1$, $(H_2, H_3) = (H_z, H_{zz})$, ξ = 1/We, and $\mu^2 = Ce - 3$ are the deviation variables, and Ca = 1/(ReWe)

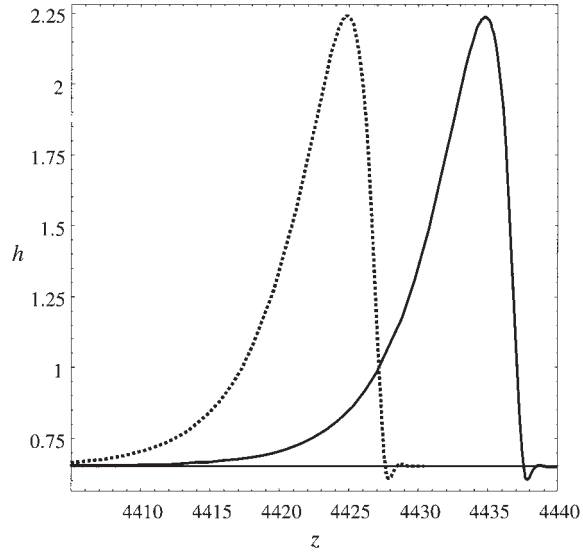

Figure 11. Solitary wave profiles.

The solid curve was obtained by time simulations with a monochromatic pulsing frequency of f = 0.016, and Re = 20.47, We = 1, β = 90°. The dashed curve is the corresponding homoclinic profile. Celerity from time simulations is Ce = 3.492, whereas that corresponding to the homoclinic orbit is Ce = 3.492.

is the capillary number. The upper branch h_u has been approximated by $h_u = 1 + \mu/\sqrt{3} + \mu^2/9$. The linear and quadratic components of the vector field are given by **L** and **Q**, respectively. In the 3D phase space (H_1, H_2, H_3) we have a 2D center manifold (resulting from the double zero) and a 1D stable manifold spanned by the eigenvectors corresponding to the zero eigenvalues and negative eigenvalue, respectively. The long-term dynamics of flow in phase space near the origin is governed by the flow on the center manifold. The flow on the center manifold is obtained by adding two trivial equations, $\dot{\mu} = 0$ and $\dot{\zeta} = 0$ to Eq. 31, and on using the center manifold theorem, we may approximate the tangent space near $\mu \to 0$ and $\zeta \to 0$ by

$$\dot{H}_1 = H_2 \tag{34}$$

$$\dot{H}_2 = -H_1^2 + \frac{H_2 H_1}{18\mathrm{Ca}} - \frac{2\mu H_1}{\sqrt{3}} + \frac{(19818\mathrm{Ca}^2 - 35)H_2^2}{22{,}680\mathrm{Ca}^2} + \frac{\mu H_2}{18\sqrt{3}\mathrm{Ca}} - \frac{\zeta H_2}{10\mathrm{Ca}} \tag{35}$$

Normal form analysis of the above dynamical system, using the procedure outlined by Nguyen and Balakotaiah,[12] further simplifies the equations. Generic flow equations of the following form may be expressed as

$$\dot{H}_1 = H_2 \tag{36}$$

$$\dot{H}_2 = \mathrm{AA}H_1^2 + \mathrm{CC}\mu H_1 + \frac{\mathrm{BB}H_2 H_1}{\mathrm{Ca}} + \left(\frac{\mu \mathrm{D1}}{\mathrm{Ca}} + \mathrm{D2Re}\right)H_2 \tag{37}$$

where the coefficients AA, BB, CC, D1, and D2 are model dependent. Further, using Melnikov's analysis for homoclinic orbits, as described in Nguyen and Balakotaiah,[12] we may obtain useful correlations for the peak height and speed of the solitary waves. Using Eq. 37 results in the following expressions for $h_{\max}$, the peak height, and Ce, the celerity of the solitary wave:

$$h_{\max} - 1 = \frac{7\mathrm{CCD2}}{2(\mathrm{BBCC} - 7\mathrm{AAD1})\mathrm{We}} \tag{38}$$

$$Ce - 3 = \frac{7\mathrm{AAD2}}{(\mathrm{BBCC} - 7\mathrm{AAD1})\mathrm{We}} \tag{39}$$

By dividing the above two equations, we may derive a relation for the peak height and speed of solitary waves. The linear speed–height relation is expressed as

$$Ce - 3 = 2\,\frac{\mathrm{AA}}{\mathrm{CC}}\,(h_{\max} - 1) \tag{40}$$

Using the flow given by Eq. 35 leads to the following equations for peak height, speed, and the height–speed relation:

$$h_{\max} - 1 = \frac{63}{25\mathrm{We}} = \frac{2.52}{\mathrm{We}} \tag{41}$$

$$Ce - 3 = \frac{63\sqrt{3}}{25\mathrm{We}} = \frac{4.365}{\mathrm{We}} \tag{42}$$

and

$$Ce = \sqrt{3}h_{\max} + 3 - \sqrt{3} \tag{43}$$

For inclined films, the procedure leads to

$$h_{\max} - 1 = \frac{63}{25}\,\frac{\mathrm{Re} - \mathrm{Re}_c}{\mathrm{ReWe}} = 2.52\,\frac{\mathrm{Re} - \mathrm{Re}_c}{\mathrm{ReWe}} \tag{44}$$

$$Ce - 3 = \frac{63\sqrt{3}}{25}\,\frac{\mathrm{Re} - \mathrm{Re}_c}{\mathrm{ReWe}} = 4.365\,\frac{\mathrm{Re} - \mathrm{Re}_c}{\mathrm{ReWe}} \tag{45}$$

and

$$Ce - 3 = \sqrt{3}(h_{\max} - 1) \tag{46}$$

Equations 44 and 45 are valid for Reynolds numbers beyond the critical Reynolds number, $\mathrm{Re}_c = 10/[3\cot(\beta)]$. Our model given by Eq. 15 predicts that the speed and peak height of the solitary waves are related linearly and that the slope of the speed–height line is $\sqrt{3}$. Experimental slopes deduced from Liu and Gollub[4] give values between 1.7 and 2. Recent experiments by Tihon et al.[13] give a value of 1.8 for the slope. Although the derivation shown above is valid only in the vicinity of the critical flow rate, the correlations, especially the slope of the speed–height linear relation, seem to have a much larger validity range. The relationship shown by Eq. 43 is novel and predicts experimental slopes with reasonable accuracy. Similar analysis of equations derived in Ooshida,[14] Ruyer-Quil and Manneville,[6] and Panga and Balakotaiah[15] yield the same relations as that given by our model Eq. 15. Finally, it should be pointed out that the relation given by Eq. 46 is independent not only of the angle of inclination but also of the fluid properties and flow rate.

Summary and Discussion

A new two-mode model that can describe the dynamics of inclined and vertically falling films for $\mathrm{We} > 1$ is presented. The model is validated by comparing its predictions with those corresponding to direct numerical simulations. Time simulations of the model for monochromatic inlet forcing frequencies showed that the speed and peak height relation for solitary waves is linear and is in quantitative agreement with experimental data. We presented a new family of traveling waves that correspond to the solitary waves obtained in the limit of very low frequency excitation. Weakly nonlinear analysis of the new wave family shows that the speed–peak height linear relation for solitary waves has a slope of $\sqrt{3}$, which is in close agreement with experimentally determined slopes.

We now discuss some limitations and extensions of the model presented here. In deriving the model, we assumed a

self-similar velocity profile. However, recent experiments and DNS of 2D film flow equations show that the velocity profile is not parabolic in a small region between the main hump and the first capillary wave. Tihon et al.[13] and Malamataris et al.[16] show that wall shear stress is negative and there is flow reversal in this small region. The h–q model presented here predicts this feature (negative q) qualitatively. Further discussion on the accuracy of the h–q model can be found in Mudunuri.[8]

The boundary conditions used in the simulations can be improved by using the kinematic condition given by Eq. 4, to evaluate $q_x(0, t)$. However, for small-amplitude perturbations, the final wave profiles are not influenced by the boundary conditions.

The two-equation models, such as the Shkadov model,[5] that do not include the streamwise viscous terms cannot predict the speed–peak height relation derived here.

The two-equation model presented here is also used to study wave interactions and multifrequency (commensurate and incommensurate) inlet forcing. The results compare favorably with experimental observations. Further details can be found in Mudunuri.[8]

Acknowledgments

This work was partially supported by a NASA Glenn Research Center Grant NNC05GA42G.

Literature Cited

1. Kapitza PL, Kapitza SP. Wave flow in thin layers of a viscous fluid. *Zn Eksper Teor Fiz.* 1949;19:105.
2. Chang HC. Wave evolution on a falling film. *Annu Rev Fluid Mech.* 1994;26:103.
3. Alekseenko SV, Nakoryakov VY, Pokusaev BG. Wave formation on a vertical falling liquid film. *AIChE J.*1985;31:1446-60.
4. Liu J, Gollub JP. Solitary wave dynamics of film flows. *Phys Fluids.* 1994;6:1702-1712.
5. Shkadov VYa. Wave flow regimes of a thin layer of viscous fluid subject to gravity. *Izv Ak Nauk SSSR Mekh Zhi Gaza*. 1967;2:43-51.
6. Ruyer-Quil C, Manneville P. Improved modeling of flows down inclined planes. *Eur Phys J B.* 2000;15:357-369.
7. Pumir A, Manneville P, Pomeau Y. On solitary waves running down an inclined plane. *J Fluid Mech.* 1983;135:27-50.
8. Mudunuri RR. *Dynamics of Free Falling Thin Viscous Films*. PhD thesis. Houston, TX: University of Houston; 2006.
9. Nosoko T, Miyara A. The evolution and the subsequent dynamics of waves on a vertically falling liquid film. *Phys Fluids.* 2004;16:1118.
10. Liu J, Paul JD, Gollub JP. Measurements of the primary instabilities of film flows. *J Fluid Mech.* 1993;250:69-101.
11. Argyriadi K, Serifi K, Bontozoglou V. Nonlinear dynamics of inclined films under low-frequency forcing. *Phys Fluids.* 2004;16:2457-2468.
12. Nguyen LT, Balakotaiah V. Modeling and experimental studies of wave evolution on free falling viscous films. *Phys Fluids.* 2000;12:2236.
13. Tihon J, Serifi K, Argyriadi K, Bontozoglou V. Solitary waves on inclined films: Their characteristics and the effects on wall shear stress. *Exp Fluids.* 2006;41:79-89.
14. Ooshida T. Surface equation of falling film flows which is valid even far beyond the criticality. *Phys Fluids.* 1999;11:3247.
15. Panga MKR, Balakotaiah V. Low-dimensional models for vertically falling viscous films. *Phys Rev Lett.* 90;154501:2003.
16. Malamataris NA, Vlachogiannis M, Bontozoglou V. Solitary waves on inclined films: Flow structure and binary interactions. *Phys Fluids.* 2002;14:1082-1094.

Manuscript received Jun. 5, 2006, and revision received Aug. 27, 2006.